



Dual role of Fe boost lattice oxygen oxidation of Mo-based materials from kinetics and thermodynamics

Qingcui Liu^a, Qiaohong Su^a, Wenhua Cheng^a, Juan Ding^a, Wenjun Zhang^{b,*}, Jiulin Wang^a, Yonggang Wang^{c,*}, Xingchao Wang^a, Yudai Huang^{a,*}

^a State Key Laboratory of Chemistry and Utilization of Carbon Based Energy Resources, College of Chemistry, Xinjiang University, Urumqi, 830017, Xinjiang, PR China

^b Center of Super-Diamond and Advanced Films (COSDAF), and Department of Materials Science and Engineering, City University of Hong Kong, Hong Kong, PR China

^c Department of Chemistry and Shanghai Key Laboratory of Molecular Catalysis and Innovative Materials, Institute of New Energy, iChEM (Collaborative Innovation Center of Chemistry for Energy Materials), Fudan University, Shanghai, 200433, PR China

ARTICLE INFO

Keywords:

Mo₂C
Dual role of Fe
Electrocatalyst
Lattice oxygen oxidation
Oxygen evolution reaction

ABSTRACT

High-valent Mo-based oxides are easily dissolved in alkaline electrolyte resulting in complete surface reconstruction of catalyst. Therefore, there are few researches on the oxygen evolution reaction (OER) process of this material, especially the reaction mechanism. Herein, Fe-Mo₂C@CN was synthesized by introducing 3d metal Fe into the Mo-based catalyst, which inhibited the complete dissolution of Mo. The overpotential is only 226 mV at a current density of 10 mA cm⁻². Experimental and density functional theory (DFT) results demonstrate that excellent electrocatalytic performance derives from the dual role of Fe and the thermodynamically favorable single-site lattice oxygen oxidation mechanism (LOM). Electronic-rich pure Fe inhibits the molybdenum dissolution while enhancing the reaction kinetics. And the doped Fe decreases the d-band center, weakens the M-O (metal-oxygen) bond, and promotes the involvement of lattice oxygen in the OER process. This work provides theoretical basis for the engagement of Mo-based catalysts in water splitting.

1. Introduction

Electrolysis of water to produce hydrogen is an effective way to achieve green hydrogen, laying the foundation for deep decarbonization [1,2]. It consists of two primary components, the hydrogen evolution reaction (HER) at the cathode and the oxygen evolution reaction (OER) at the anode. Among them, OER is a 4-electron-proton transfer process with sluggish reaction kinetics and high overpotential, hindering the development of electrolytic water technology [3,4]. Therefore, researchers have exerted much endeavor in facilitating the OER process [5,6]. Currently, the majority of reported OER processes obey the adsorption evolution mechanism (AEM) [7,8]. However, the high overpotential for the rate-determining step (RDS) of OOH* formation into O-O cannot reasonably explain the reported low overpotential of some metal oxides [9]. Therefore, the lattice oxygen oxidation mechanism (LOM) was proposed [10], denoting a hybridization process of oxygen non-bonded states (O_{NB}) in adjacent oxygen atoms (O²⁻), where the reaction rate relies on the coupling of the O-O bonds of the lattice oxygen atoms. The OER electrocatalyst for the LOM process has a

distinct edge in reaction rate compared to AEM [11]. However, the mechanism has currently only been mentioned in metal oxides. In the alkaline environment, OER catalysts are pre-catalysts and the active phase will form the corresponding oxides/hydroxides [12–14]. For some highly oxidizable metals, the catalyst surface is reconfigured to form lattice oxygen with the generation of oxygen during the OER process. Such materials can therefore be further investigated as potential OER catalysts that follow LOM.

Since the d-band center and Fermi energy level of molybdenum carbide are extremely similar to Pt, it is a good HER electrocatalyst in itself [15,16]. The study of the OER process of molybdenum carbide is an effective approach to exploring bifunctional catalysts, which can reduce the complexity and cost of water electrolysis [17,18]. And the significant challenge in the investigation of this process is the inhibition of the complete dissolution of Mo in the OER process and the analysis of the reconstituted samples. However, we noticed that along with the progress of OER, the generation of oxygen and OH⁻ adsorption, a steady source of lattice oxygen is formed around the Mo atom, which can be a candidate for the active center of the OER process with LOM. It has been

* Corresponding authors.

E-mail addresses: apwjzh@cityu.edu.hk (W. Zhang), ygwang@fudan.edu.cn (Y. Wang), huangyd@xju.edu.cn (Y. Huang).

<https://doi.org/10.1016/j.apcatb.2023.123188>

Received 24 June 2023; Received in revised form 9 August 2023; Accepted 18 August 2023

Available online 20 August 2023

0926-3373/© 2023 Elsevier B.V. All rights reserved.

demonstrated that mixing 3d transition metals (TM) and high valence non-3d metals can effectively optimize the electronic structure of metals [19]. The 3d orbital of the TM and the 2p orbital of O reach a suitable degree of hybridization to promote the accessibility of the oxygen non-bonded state during LOM [10], which consequently enhances the OER properties of the material. Recently, electronic-rich properties of metallic Co have also been reported to suppress the dissolution of molybdenum carbide [20].

On this basis, this work introduces Fe into Mo₂C to form small-sized Fe-Mo₂C encapsulated in the N-doped carbon nanosheets (Fe-Mo₂C@CN). Interestingly, the presence of Fe not only inhibited the dissolution of molybdenum, but the dual role of Fe makes different contributions in the OER process. Pure Fe improves the electrical conductivity of the material and enhances the reaction kinetics of the OER process. While Fe doping into the lattice further improves the electronic structure of the material, the d-band center shifts downward, allowing the antibonding orbitals of M-O (metal oxygen) to be filled and activating the lattice oxygen. The O_{NB} loses electrons and undergoes an oxidation reaction, which achieves lattice oxygen oxidation. The overpotential of Fe-Mo₂C@CN reaches 226 mV at a current density of 10 mA cm⁻² with favorable stability. Simultaneously, single and dual site assumptions were made to investigate the reaction sites of Fe-Mo₂C@CN in the OER process, respectively. It was verified by theoretical calculations that the Mo-based material is thermodynamically more favorable at the single site and follows the reaction mechanism of LOM in the OER process. This paper proposes the OER mechanism of molybdenum carbide, which lays the foundation for the application of this material in electrocatalyst and opens up a new direction for the development of OER nanoelectrocatalysts, expanding the application of Mo-based materials in electrolytic water.

2. Experimental section

2.1. Sample synthesis

2.1.1. Synthesis of M-Mo₂C@CN

In the typical procedure, a certain amount of (NH₄)₆Mo₇O₂₄ (0.4824 g) was dissolved in 30 mL of deionized water under sonication to form solution A. 0.1608 g of Fe(NO₃)₃•9H₂O was dissolved in 10 mL of deionized water to form solution B. Solution B was poured into solution A with stirring and continuing to stir for 30 min. Subsequently, 2.8377 g of melamine (MA) was added and further stirred for 6 h. The above mixture was transferred into the sand core funnel, and vacuum filtration was employed to make the solid-liquid separation, washed with deionized water 3 times, and vacuum-dried at 80 °C for 12 h to obtain solid samples. The collected yellowish powder sample was placed in a tube furnace in N₂ at a heating rate of 2 °C min⁻¹ to 400 °C and maintained for 1 h. Then, the sample was continued to heating to 900 °C with a heating rate of 5 °C min⁻¹ and sustained for 2 h to obtain Fe-Mo₂C@CN.

Under the same conditions of the experimental procedure, Fe (NO₃)₃•9H₂O was replaced by the same mole amount of Co (NO₃)₂•6H₂O and Ni(NO₃)₃•6H₂O to obtain the corresponding Co-Mo₂C@CN and Ni-Mo₂C@CN, respectively. Mo₂C@CN was obtained without the addition of Fe(NO₃)₃•9H₂O, and Fe@CN was achieved without the injection of (NH₄)₆Mo₇O₂₄.

2.1.2. Synthesis of Fe-Mo₂C@CN-X

Under the same conditions of the experimental procedure, the samples Fe-Mo₂C@CN-700, Fe-Mo₂C@CN-800, Fe-Mo₂C@CN-900, Fe-Mo₂C@CN-1000 were obtained which correspond to a secondary calcination temperature of 700, 800, 900, and 1000 °C in the synthesis of Fe-Mo₂C@CN.

2.1.3. Synthesis of Fe free-Mo₂C@CN

An excess of concentrated hydrochloric acid was added to a quantity of Fe-Mo₂C@CN, sonicated and stirred to disperse, and soaked for 48 h.

The yellow-green solution was filtered off and washed with deionized water to neutralize. Dried under vacuum at 80 °C for 12 h to obtain Fe free-Mo₂C@CN.

2.2. Materials characterization

An X-ray powder diffractometer (XRD, Bruke D8 Advance) was used to characterize the physical phase and crystal structure of the samples. The radiation source was a Cu Kα target (λ = 0.154056 nm), and the scanning angle was 5°–80°. Raman (HORIBA, HR Evolution) and Fourier transform infrared spectroscopy (FT-IR, Bruke, VERTEX 70 RAMI) analysis was performed on the structure of the samples. A field emission scanning electron microscope (SEM, Hitachi, S-4800) and a transmission electron microscope (TEM, FEI Tecnai G2 F20) were used to analyze the morphology and microstructure of the samples. Energy dispersive spectrometry (EDS) was used to feature the distribution and content of elements in the samples. An X-ray photoelectron spectrometer (XPS, Thermo Fisher, Thermo Scientific K-Alpha+) and ultraviolet photoemission spectroscopy (UPS) were applied to characterize the composition and chemical state of the samples, with an excitation source of Al Kα rays, etched at different depths by Ar⁺ ions, and all XPS spectra were obtained after calibration with C 1s spectra at 284.6 eV. The UPS tests were preceded by Au calibration. The inductively coupled plasma-mass spectrometry (ICP-MS, Agilent 7900) was applied to detect the content of metal elements in the electrolyte. The calcination process was analyzed by thermogravimetry (TG, Hitachi, STA 7300).

2.3. Electrochemical measurements

All electrochemical measurements were carried out on CHI-760D electrochemical workstation in 1 M KOH (pH = 13.6). The Ag/AgCl electrode as the reference electrode, a carbon rod as the counter electrode and nickel foam (NF) (1 × 1 cm²) with catalyst as the working electrode. The catalyst ink liquid was prepared as the following steps: 3.5 mg active material was dispersed in 1.11 mL mixed solvent containing deionized water and ethanol in volume ratio of 5 : 6 with 10 μL 5 wt% Nafion. Then the suspension was treated by ultrasonication for about 15 min to make it evenly distributed. 100 μL catalyst ink was added dropwisely onto NF with pipette, and the electrodes were dried at room temperature overnight before use.

The cyclic voltammetry (CV) was conducted for several cycles to stable the system until it kept steady. Then, the linear sweep voltammetry (LSV) was recorded at 10 mV s⁻¹ to evaluate electrocatalytic performance from 0 to 0.8 V for OER. All the potentials E as x axis were transformed relative to reversible hydrogen electrode (vs. RHE) according the equation $E_{(vs. RHE)} = E_{(vs. Ag/AgCl)} + 0.05916 \times pH + 0.197$ V, in which $E_{(vs. Ag/AgCl)}$ is applied potential versus Ag/AgCl, 0.197 is the standard electrode potential of Ag/AgCl at 25 °C, and pH is 13.6 for 1 M KOH measured by pH meter. The overpotential η of OER is calculated by $\eta = E_{(vs. RHE)} - 1.23$ V. All measured current values are divided by the area of working electrode to obtain the corresponding current density (j) as y axis. Tafel curves were transformed and calculated from the LSV curve around the current density 10 mA cm⁻². Wherein, the transverse axis is obtained by taking the logarithm of j measured by LSV, the vertical axis is the overpotential η straight lines are fitted by formula $\eta = \log|j| + a$, here b is the Tafel slope for a definite sample. The electrochemical active surface area (ECSA) of electrocatalyst is obtained via double layer capacitance C_{dl}, which can be acquired by measuring the CV curves at varied scan rates of 10, 30, 50, 70, and 100 mV s⁻¹ with the potential from 1.22 to 1.32 V (vs. RHE) in the non-faraday potential region, where the charge transfer on the electrode is considered negligible, and the current is mainly generated by the charge and discharge of the double layer. The current density difference (Δj) is obtained by calculating the difference of j for each charge and discharge curve at 1.27 V vs. RHE. By plotting Δj versus scan rate, the slope of the fitting straight line is C_{dl}. The electrochemical impedance spectroscopy (EIS)

was also conducted at the $E_{(\text{vs. RHE})} = 1.5$ V and the alternating current amplitude 5 mV with frequency from 100 kHz to 0.01 Hz.

3. Results and discussion

3.1. Material characterizations

The synthesis of the material involves a liquid phase reaction followed by a calcination process. First of all, the coordination solution formed by Fe metal ions, ammonium ions, and molybdate is acidic, and melamine reacts with it to form precursors. After simple calcination, the melamine decomposed and curled at high temperature to encapsulate

Fe-Mo₂C in the N-doped carbon nanosheets. (Fig. 1a). For comparison, samples containing different metals (M-Mo₂C@CN) and only Mo were synthesized by the same method simultaneously, labeled as Co-Mo₂C@CN, Ni-Mo₂C@CN and Mo₂C@CN, respectively. The precursors in Fig. S1a exhibit analogous FT-IR, suggesting they have similar structures. The distinct signal peak near 817 cm⁻¹, corresponding to Mo-O-Mo, indicates the successful introduction of [MoO₄]²⁻. During high temperature calcination, at 400 °C, the melamine pyrolysis to form C₃N₄ (Fig. S2) with nanosheets structure, and the constant release of NH₃ reduces the metal to pure element [21]. It can be observed in TG diagrams of different precursors (Fig. S1b) that a plateau occurs as the temperature rises to around 400 °C, indicating that the carbon nitrides

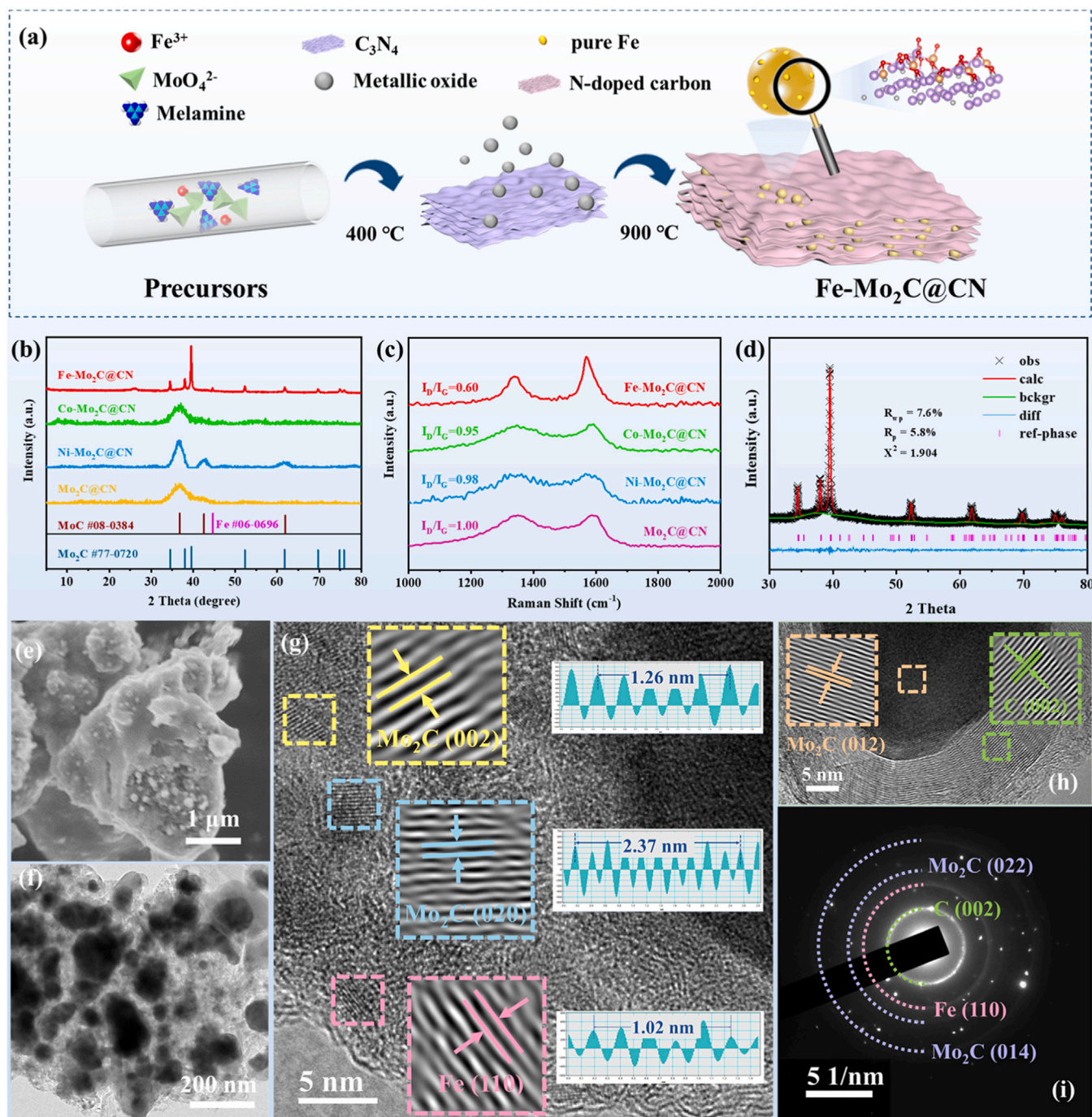


Fig. 1. (a) The schematic diagram of the synthesis process for Fe-Mo₂C@CN. (b) XRD patterns, and (c) Raman spectra of different samples. (d) Rietveld refinements of the XRD pattern, (e) SEM image, (f) TEM image, (g-h) HRTEM images and IFFT pattern, and (i) SAED pattern of Fe-Mo₂C@CN.

have been formed. When the temperature rises above 600 °C, another plateau occurs and solid phase reaction begins. M-Mo₂C gradually forms, and the N-doped carbon nanosheets are curled to encapsulate them, eventually forming M-Mo₂C@CN.

As can be seen from the XRD patterns (Fig. 1b), the sharper peak shape with the addition of Fe in comparison to several other metals (Fe/Co/Ni) indicates that the material is more crystalline, corresponding to Mo₂C (PDF#77-0702). A wide peak is present between 32° and 40° for several other samples, which can be caused by the simultaneous presence of MoC (PDF#08-0384) and Mo₂C. The difference of XRD patterns is mainly due to the different catalytic effects of different metals (Fe/Co/Ni) on Mo in the process of high temperature calcination [22]. Since the target product corresponds to Mo₂C and the synthesis method is the same either Ni/Co is introduced or not. And they are all mixed phases of MoC and Mo₂C (Fig. 1b), so they are all denoted by Mo₂C for the convenience of comparison later in the paper. However, due to the low Fe content, a weaker peak appears in the XRD spectra at 44.67° corresponding to the (110) crystal plane of pure Fe. High-temperature calcination is usually associated with the formation of carbon material, so Raman analysis was performed. The peak at 1342 cm⁻¹ in Fig. 1c matches the D-peak and is due to the disordering of the sp² hybridised carbon atoms. The peak at 1580 cm⁻¹ matches the G-peak and is attributed to graphitic carbon vibrations. The value of I_D/I_G ratio reflects the degree of graphitization of the material. Fe-Mo₂C@CN corresponds to the smallest I_D/I_G value in the diagram, indicating the highest degree of graphitization and electrical conductivity among the M-Mo₂C@CN materials. The Rietveld refinement of the XRD pattern of Fe-Mo₂C@CN (using GSAS software) is shown in Fig. 1d. And the corresponding lattice parameters are shown in Table S1. The reduced average Mo-C bond length relative to standard Mo₂C is probably due to the doping of N and Fe atoms. And the N atom can be easily inserted into the gap positions of the transition metal atoms. The introduction of N atoms stabilizes the structure of Mo₂C and makes it less susceptible to corrosion at high overpotential [23].

Further analysis of the morphology and composition of Fe-Mo₂C@CN exhibit a smaller nanoparticle structure with a surface wrapped in N-doped carbon nanosheets (Fig. 1e and f). As shown in

Fig. 1g-i, the high-resolution transmission electron microscope (HRTEM) images and inverse fast Fourier transform (IFFT) pattern of Fe-Mo₂C@CN affirm the presence of Mo₂C, graphitic carbon layers and a slight amount of pure Fe. The various layer spacing of 0.20, 0.25, 0.23, 0.22, and 0.34 nm in Fig. 1g-h correspond to the (110) crystal plane of Fe, the (002), (020), and (012) crystal planes of Mo₂C, and the (002) crystal plane of graphitic carbon, respectively. This also reaffirms the formation of pure Fe on the surface.

3.2. Electrocatalytic OER performance

The electrocatalytic performance of M-Mo₂C@CN for OER was initially evaluated in 1 M KOH solution (Fig. 2a). It can be seen that the introduction of Fe has the most pronounced effect on the catalyst activity. At a current density of 10 mA cm⁻², the overpotential of Fe-Mo₂C@CN reaches 226 mV, which is better than that of the Mo-based material after the introduction of Ni or Co. The Tafel slope reflects the activity of the catalyst from a catalytic mechanism perspective. Fe-Mo₂C@CN has the lowest Tafel slopes (40.2 mV dec⁻¹) in Fig. 2b, indicating optimal catalytic activity. Comparing the two parameters, which measure OER performance, with molybdenum carbide in the literatures, it can be seen that the material is at the top of the range (Fig. 2f), indicating that this material has excellent OER performance. Further investigation of the reaction kinetics of the OER process was carried out by performing EIS tests on these samples and simulating an equivalent circuit as shown in Fig. 2c. For the equivalent circuit, R_s is the resistance of the uncompensated solution, and R_p is the charge transfer resistance at the interface between the electrolyte solution and the electrode. It is observed that the EIS results are in general accordance with the OER performance. The R_p of Fe-Mo₂C@CN is only 1.92 Ω, smaller than that of the other samples (Table S3) in the Supporting Information for specific data for the different samples after fitting, corresponding to the smallest semicircular diameter in Fig. 2c. To interpret the correlation between the catalyst activity and its active surface area, the ESCA of the catalyst was measured for comparison. Δj is linearly related to the scan rate with a slope of C_{dl}, and which is proportional to the ESCA, so the ESCA can be compared by the C_{dl} value. As can be seen

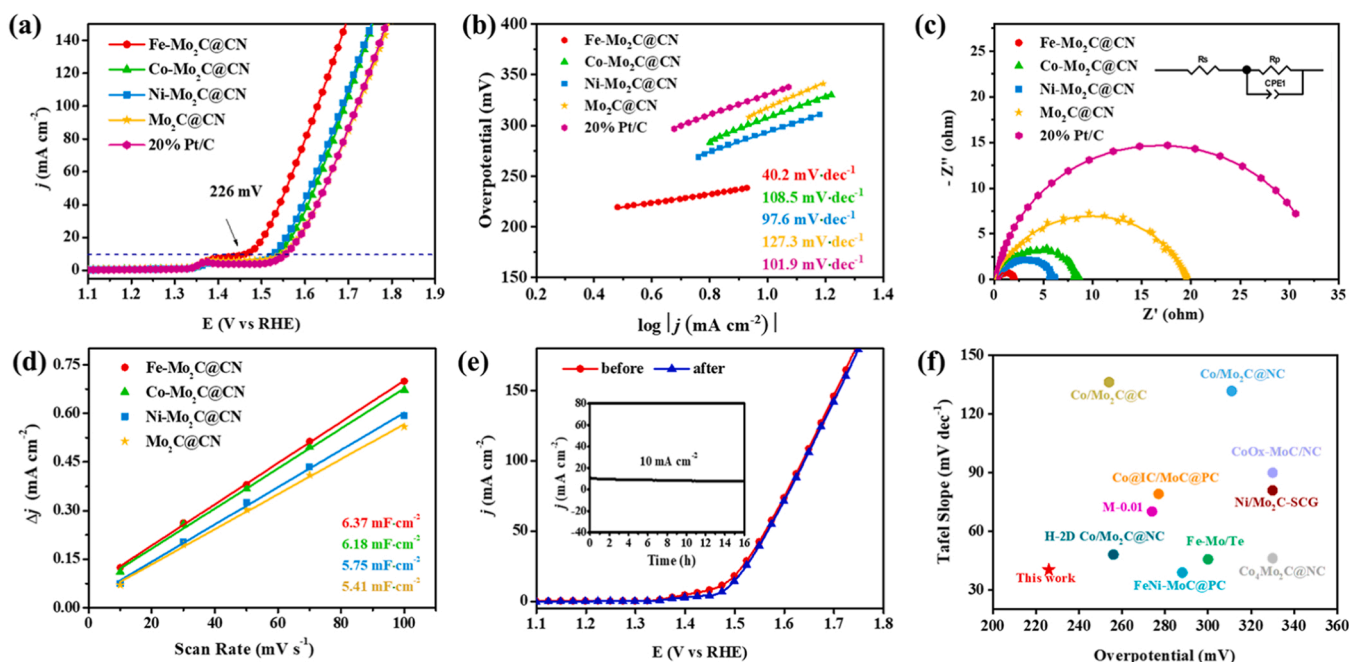


Fig. 2. (a) LSV curves, (b) Tafel curves, (c) EIS curves, and (d) the linear relationship between current density and the scanning rate for M-Mo₂C@CN. (e) LSV curves before and after stability test for Fe-Mo₂C@CN (the illustration is the chronoamperometric stability curve). (f) OER activity comparison of overpotential at 10 mA cm⁻² and Tafel slopes for M-Mo₂C@CN and some molybdenum carbide-related catalysts (Table S2).

from Fig. 2d. Fe-Mo₂C@CN corresponds to the largest C_{dl}, which would indicate that its ESCA is the largest. This is also related to the homogeneous morphological structure of the material, where smaller nanoparticles can also expose more active sites.

Stability is also one of the important factors in evaluating the performance of the catalyst. Fig. 2e shows the LSV plot before and after the stability test, and it can be seen that there is a slight decrease in properties at small currents, which may be due to the material being partially dissolved and reconstituted, and the reaction mechanism will be further analyzed later in the paper. The inset shows the measured chronoamperometric stability curve, which was obtained at a voltage of 1.45 V (vs. RHE). No obvious downward trend in the curve can be seen during the test, indicating that the material maintained good stability during the OER. After manual compensation of the LSV curves of Fe-Mo₂C@CN, the corresponding overpotential is only 287 mV when the current density is 100 mA cm⁻² (Fig. S5a). The material was then further tested for its stability over long periods, testing the OER performance of the same sample every other week. The overpotential is found to be stable around 226 mV at a current density of 10 mA cm⁻², which is stable at the same level during one month of continuous testing (Fig. S5b).

Calcination temperature is one of the main conditions that affect the properties of the material. For molybdenum carbide, different materials can be obtained at different calcination temperatures [24]. The carbonization temperature of the material is usually considered to be above 700 °C. Therefore, Fe-Mo₂C@CN synthesized at different temperatures (700–1000 °C) was investigated by XRD. As can be seen in Fig. S6a, At 700 °C, there is a very distinct peak of MoC near 37° (Fig. S6a), indicating that at this time it is MoC and Mo₂C, at 800 °C this peak disappears, and the peak at 61.9° of MoC is still present regardless of at 700 °C or 800 °C, but the peak at 61.9° disappears at 900 °C, and MoC completely transforms into Mo₂C. This means that at less than 900 °C, the material is a mixture of MoC and Mo₂C. From the Raman spectra (Fig. S6b), it can be seen that Fe-Mo₂C@CN-900 has the highest graphitization at 900 °C. The SEM images of the material at different temperatures show that the wrapped small particles develop gradually with smaller particle diameters as the temperature increases, but the material is completely crushed when the temperature rises to 1000 °C

(Fig. S7). Being the electrocatalyst, Fe-Mo₂C@CN-900 has the best electrocatalytic performance among the samples (Fig. S8). Hence, the optimal synthesis temperature of Fe-Mo₂C@CN is 900 °C (All of the Fe-Mo₂C@CN discussed in the context refers to Fe-Mo₂C@CN-900).

3.3. Exploration of the active center

To further investigate the reaction mechanism of Fe-Mo₂C@CN and its active center, the pure Fe on the surface was removed by acid etching as a comparison sample. To ensure clean removal, Fe free-Mo₂C@CN was obtained in this paper after 48 h of acid etching. The color of the solution after acid washed appears yellow-green, indicating that the surface layer is mainly pure Fe (Fig. S12). The XPS full spectrum of Fe free-Mo₂C@CN (Fig. 3a) shows the disappearance of the Fe peak near 711 eV, indicating that the surface pure Fe was successfully removed. Interestingly, in the high-resolution XPS spectra of Fe, the peaks corresponding to pure Fe disappear, but a few amounts of +2 and +3 valence Fe are still present, which suggests partial Fe adulteration (Fig. S13a). The detailed spectra of all other atoms corresponding to the subpeaks show no significant changes, indicating that the acid treatment had no noticeable effect on the other atoms and structures (Fig. S13b-d, Table S4). Subsequently, the internal metallic elements of the material were analyzed by argon ion etching (Fig. S14). The valence state of Fe is almost constant at various depths as can be seen in the Figure, which reaffirms the partial Fe doping into Mo₂C. And this is also consistent with the Mo-C bond length variation in the XRD Rietveld refinement.

Comparing the electrocatalytic performance of the samples before and after acid etching, it is clear that the OER performances of Fe@CN and Mo₂C@CN are only better than that of blank NF and much lower than those of Fe-Mo₂C@CN and Fe free-Mo₂C@CN, whereas Fe free-Mo₂C@CN is only slightly lower than that of Fe-Mo₂C@CN (Fig. 3b). These indicate that the pure Fe on the surface removed by acid etching does not play a dominant role in the OER process, while the doped Fe atoms and Mo₂C are the main active centers. Also, it implies that Mo₂C in the material also has catalytic activity and not just as a combined modifier [25]. Further analysis of the ESCA and EIS properties of both samples (Fig. 3c, d) reveals that the corresponding impedance values differed significantly (Table S3), but the active surface area differed less,

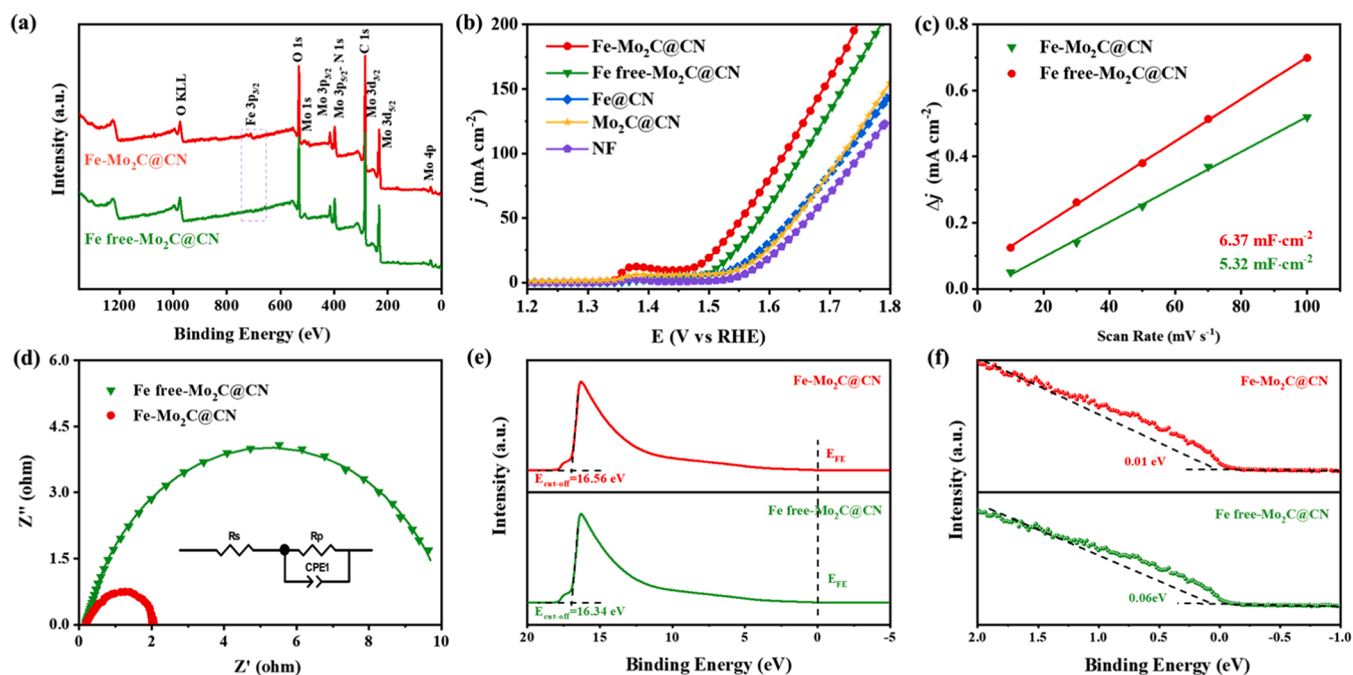


Fig. 3. (a) The XPS full spectrum, (b) LSV curves, (c) the linear relationship between current density and the scanning rate, and (d) EIS curves for Fe-Mo₂C@CN and Fe free-Mo₂C@CN. (e) The maximum value of valence band, and (f) work function for the different samples.

which suggested that the pure Fe surface layer mainly enhance the reaction kinetics. From the later analysis, it is evident that partial doping of Fe into the Mo_2C crystal matrix results in excellent electrocatalytic properties of Fe free- $\text{Mo}_2\text{C}@\text{CN}$.

We analyzed the electronic supply capacity of both materials by UPS tests to illustrate the origin of the fast kinetics (Fig. 3e, f). The smaller the value of the work function (Φ), the lower the energy barrier needed to release electrons from the material surface to the vacuum energy level, the more favorable the reaction kinetics. The closer valence band top to the Fermi energy level demonstrates that the surface exposes more metallic properties and has a higher density of states near the Fermi energy level. The valence band top and Φ of both samples are similar, with Fe free- $\text{Mo}_2\text{C}@\text{CN}$ ($\Phi = 4.94$ eV) slightly larger than Fe- $\text{Mo}_2\text{C}@\text{CN}$ ($\Phi = 4.62$ eV), which is consistent with the electrocatalytic performance. It illustrates that the removed surface layer of pure Fe enlarges the metallicity of the material, effectively regulates the electronic states on the catalyst surface, and enhances the reaction kinetics of the OER process.

The whole OER process and the reconstructed catalyst structure were well optimized with the comparison of the changes of electrode materials and electrolytes before and after the reaction. The amount of metal ions in the electrolyte during the reaction (Fig. S15a) shows that Fe is almost not dissolved with the reaction, and Mo will be partially dissolved. However, the reconstitution process occurs mainly in the first cycle of the CV scan (Fig. S15b) [13]. EDS and XPS analyses show that Fe- $\text{Mo}_2\text{C}@\text{CN}$ contains elements of Fe, Mo, C, N, and O (Fig. 3a, S15c, and S16a). After OER, the Mo element is significantly reduced. For the EDS analysis of Fe free- $\text{Mo}_2\text{C}@\text{CN}$ after the reaction (Fig. S15d), the Mo and Fe atomic ratio is close to 1 : 1, which also indicates that the material surface was reconstructed during the OER process.

To investigate the relevant composition and changes in the various chemical terminal species on the surface of Fe- $\text{Mo}_2\text{C}@\text{CN}$ before and after the OER process, XPS tests were carried out on the material. From

the Fe 2p signal fitting, it is observed that Fe- $\text{Mo}_2\text{C}@\text{CN}$ is mainly composed of $\text{Fe}^0/\text{Fe}^{2+}/\text{Fe}^{3+}$, corresponding to the peaks of 719.9, 722.8, 725.2 eV for Fe $2p_{1/2}$ and 706.9, 709.8, 711.9 eV for Fe $2p_{3/2}$ in Fig. 4a, respectively. The existence of pure Fe again proves the metallicity of Fe- $\text{Mo}_2\text{C}@\text{CN}$, making its valence band top close to the Fermi energy level. Additionally, the two small peaks present at 715.6 and 729.9 eV correspond to two satellite peaks [12,26,27]. Comparing the XPS spectra of Fe after OER, the overall peak position is positively shifted, which may be due to the dissolution of Mo.

Mo is also a metal susceptible to being oxidized, as evident in Fig. S14, the nearer the surface layer, the more high-valent states are present in the material. The peaks at 235.6 and 232.7 eV in the Mo 3d XPS spectra of Fig. 4b are attributed to Mo^{6+} , the peaks at 232.2 and 229.0 eV are due to Mo^{4+} and Mo^{2+} corresponds to the peaks at 231.5 and 228.4 eV [28,29]. Thus, the above three valence states of Mo are present in the material. The overall peak of the XPS spectra of Mo after the OER reaction has a negative shift. This is because Mo is oxidized in the oxygen-rich environment of OER, while the dissolution of molybdenum oxide reduces the amount of high-valence Mo in the whole material, increasing electron cloud density around Mo and charge transfer. This also implies that Mo is involved in the OER process. The dissolution of Mo reduces the overall positive charge in the system and promotes the positive shift of the overall Fe 2p XPS peak. It is worth noting that after surface reconstruction, a significant increase in the O/M (oxygen/metal) ratio will increase the amount of oxygen non-bonded states [30], which favors the OER process. Notably, a large amount of Mo is dissolved from $\text{Mo}_2\text{C}@\text{CN}$ after the OER, and the +2 valence Mo disappears and is completely converted to higher valence Mo (Fig. S17), indicating that the existence of Fe reduces the dissolution of Mo. Comparison of the XPS spectra of Mo 3d before and after the introduction of Fe (Fig. S18) reveals that the introduction of Fe cause the molybdenum peak at +2 valence to shift negatively. This confirms that the introduction of Fe enhanced the electron density around molybdenum, which can provide

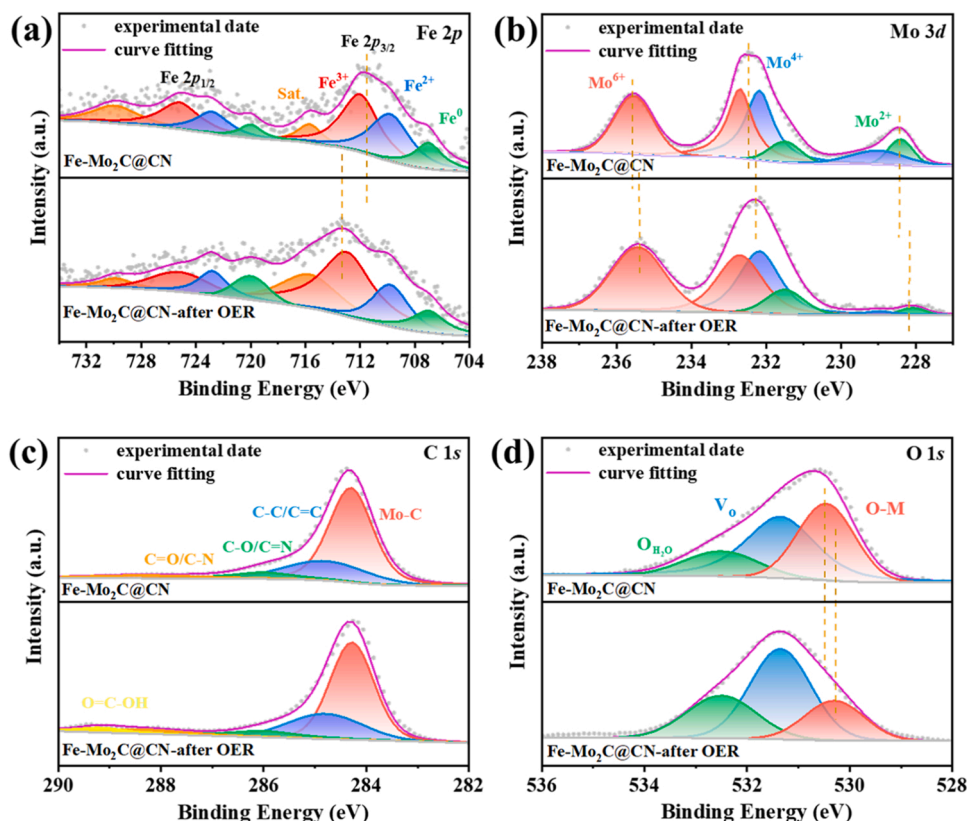


Fig. 4. High-resolution XPS spectra of Fe- $\text{Mo}_2\text{C}@\text{CN}$ before and after OER (a) Fe 2p, (b) Mo 3d, (c) C 1s, (d) O 1s.

a certain ion-shielding effect during the occurrence of OER, resulting in a moderate OH^- concentration around molybdenum, and thus suppressing the molybdenum dissolution.

It can be seen from the C 1s XPS in Fig. 4c that the corresponding subunits at 288.3, 286.0, 284.8 and 284.3 eV are allocated to the $\text{C}^{\text{O}}/\text{C}-\text{N}$, $\text{C}^{\text{N}}/\text{C}-\text{O}$, $\text{C}-\text{C}/\text{C}^{\text{C}}$, and $\text{Mo}-\text{C}$ species, respectively. The peak position of C does not change significantly after the OER reaction, but the content of C is reduced from the peak area (as shown in Fig. 4c and Table S5), which is mainly due to the fact that the C in the material is taken away by Mo when it dissolves. The appearance of these metal oxidation states is also implicated in the existence of terminal oxygen atoms, and the corresponding M-O bonds are similarly seen in the O 1s XPS spectra (Fig. 4d) at a binding energy of 530.5 eV. The peaks at 531.4 and 532.5 eV are indicative of oxygen vacancy (V_O) and adsorbed water (OH_2O) [31]. A slight negative shift in the M-O peak after the OER reaction indicates that the charge transfer around the metal is through the M-O bond, that is, electrons are transferred through the Fe-O-Mo bridge bond [32]. It can also be seen from the content of O 1s before and after the OER reaction (as shown in Table S6) that the peak area of V_O increased significantly after the reaction. During the OER process, the formation rate of surface V_O is much higher than the filling rate [33]. As a result, surface cations leach out and thus compensate for the charge balance, which process leads to surface reconfiguration. V_O is a reaction intermediate that must be produced in the LOM process, implying that the reaction mechanism of the OER process may be LOM. As the reaction occurs, the oxygen vacancy concentration and oxygen ion diffusion rate increase greatly following the dissolution of Mo, favoring O-O coupling. The N 1s XPS spectra contains a pronounced Mo-N peak (394.8 eV) in parallel to the graphitic nitrogen (401.3 eV), pyrrolic nitrogen (399.3 eV) and pyridinic nitrogen (398.1 eV) peaks in Fig. S16b [34]. There is no significant change of N element before and after OER reaction. This confirms the doping of N atoms, which would stabilize the structure of Mo_2C and reduce its solubility in alkaline solutions. The presence of pyridinic N, pyrrolic N and graphitic N all contribute significantly to the electrical conductivity of the material.

3.4. Mechanism analysis of OER progress

During the LOM process, protons and electrons are uncoupled and transferred, and the uncoupled protons are highly restricted by pH in their transfer; therefore, the LOM process is strongly dependent on the

pH of the electrolyte. The higher the pH, the more favourable the OH^- deprotonation, and the faster the reaction rate [35,36]. On this basis, the OER performance of $\text{Fe}-\text{Mo}_2\text{C}@\text{CN}$ was measured in KOH solutions at different pH (pH = 12.5, 13, 13.5, and 14) to investigate the electrocatalytic reaction principle of its process. The test results are illustrated in Fig. 5b and it can be noticed that $\text{Fe}-\text{Mo}_2\text{C}@\text{CN}$ is sensitive to pH and the performance of the material varies substantially at different pH conditions. Amazingly, the overpotential of the material reaches 190 mV at pH = 14 and a current density of 10 mA cm^{-2} . This indicates that $\text{Fe}-\text{Mo}_2\text{C}@\text{CN}$ electrocatalytic reaction follows the LOM, with the primary active center being the lattice oxygen. In order to further explore the changes of catalysts in the OER process, ex-situ Raman analysis is conducted for the process. As can be seen in Fig. 5c, two weaker peaks at 206 and 992 cm^{-1} correspond to Mo_2C , indicating that Mo_2C is stable with the progress of the OER reaction. The peak near 315 cm^{-1} corresponds to the Mo-O bond, and the shift in peak position indicates a change in the local atomic spacing, which demonstrates that the OER active site is close to Mo-O [37,38]. In addition, the peak from 470 to 700 cm^{-1} is correlated with NF (as shown in Fig. S16c). Based on the above test results of surface recognition, the possible mechanism of $\text{Fe}-\text{Mo}_2\text{C}@\text{CN}$ in the OER process is proposed (as shown in Fig. 5a). The OH^- adsorbed on the metal surface in solution first, after a proton and electron transfer process, O-O coupling occurs and eventually O_2 is released.

To thoroughly analyze the OER reaction mechanism and determine the reaction active center, DFT calculations are modeled based on the results of the previous analysis of the material tests. This part mainly investigates the role of doped Fe. Firstly, the adsorption energy of test OH at different sites is calculated to establish the beginning of the OER reaction, and the results are shown in Fig. 6a and b. It can be seen that top Mo has the strongest adsorption, followed by O2 on Fe-O-Mo bridge bond. Simultaneously, we found that the adsorption of OH at the surface metal sites is extremely strong, indicating that the material is very susceptible to oxidation under alkaline conditions. Thus, the subsequent calculations are carried out under conditions where the surface is fully oxidized. The previous experiments verify that the material follows the LOM mechanism during OER, and as there are two metals involves in $\text{Fe}-\text{Mo}_2\text{C}@\text{CN}$. Therefore, the assumptions of single and double sites are made respectively, and the calculated results are shown in Fig. 6d. As the inset of Fig. 6d demonstrates, the step diagrams corresponding to the two hypotheses overlap well, the RDS is proton transfer step and their

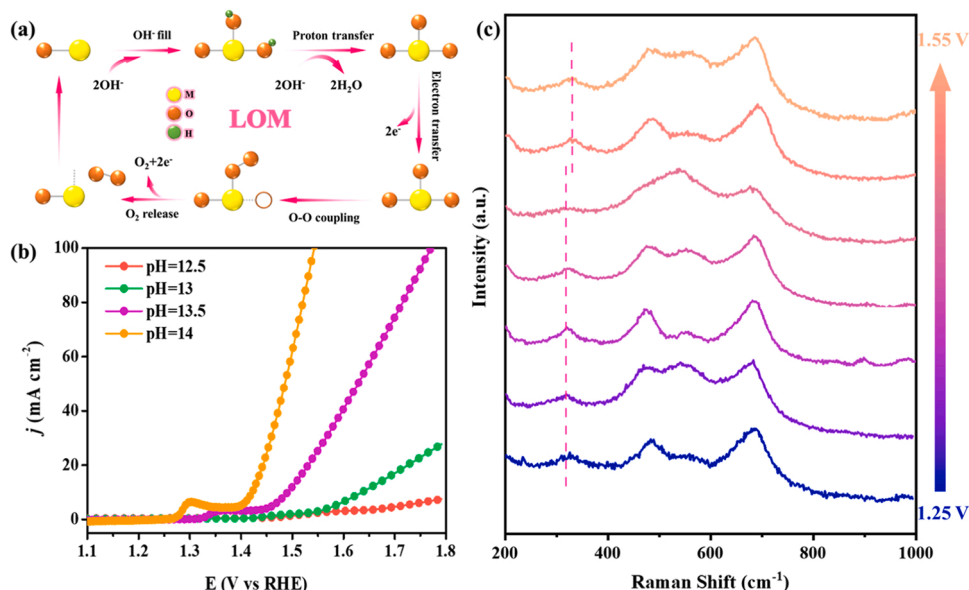


Fig. 5. (a) Reaction mechanism diagram of OER, (b) LSV curves at different pH, and (c) ex-situ Raman spectra after I-t test at different voltages of $\text{Fe}-\text{Mo}_2\text{C}@\text{CN}$.

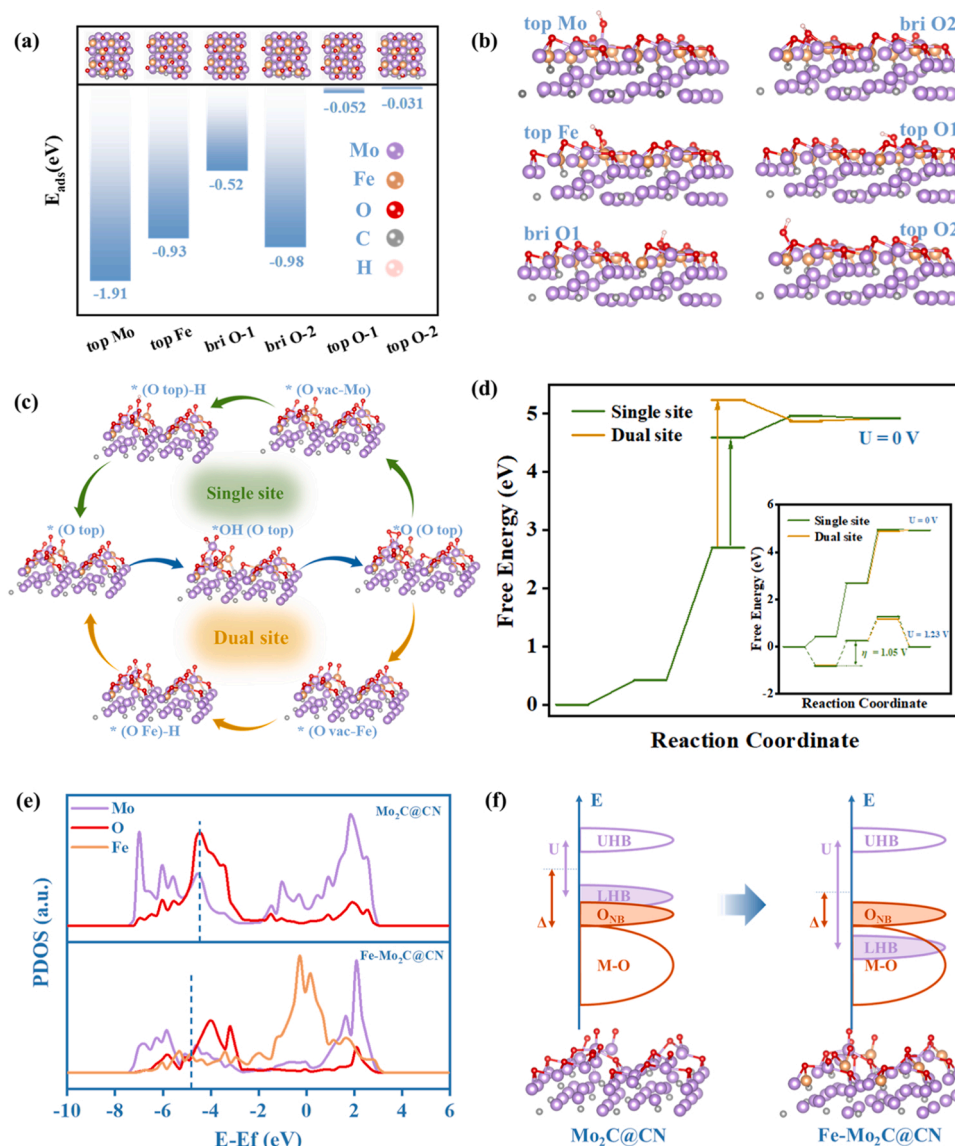


Fig. 6. (a) Adsorption energy of OH at different sites, (b) model diagram of adsorption tests at different sites, (c) diagram of the reaction process at single and dual sites, (d) diagram of the steps of the OER reaction process corresponding to single and dual sites. (e) PDOS diagram, and (f) energy level diagram of the samples.

overpotential is calculated to be 1.05 V. Nevertheless, it is evident from the thermodynamic point of view that the single site is significantly better than the dual site, indicating that the reaction process tends to favor the single site. The main active center is derived from the lattice oxygen around Mo, which is in perfect agreement with the results of the ex-situ Raman test. The OER process of Fe-Mo₂C@CN based on the AEM mechanism is also subsequently compared with the process step diagram shown in Fig. S19, with a much higher free energy of the RDS than the LOM path, which also verifies that the material follows the LOM in the OER process.

Based on the LOM mechanism, the enhanced OER process essentially reduces the adsorption of substrate for the lattice oxygen to ensure the release of reactive oxygen ligands from the lattice matrix. To achieve the triggering of lattice oxygen redox in TM oxides and (oxy)hydroxides, a large number of methods have been implemented to subtly modulate the electronic states[39]. The projected density of states (PDOS) provides a well-described electronic state of the material, and further investigation of the effect of the introduction of Fe on the active center is undertaken by comparison of the PDOS pattern analysis of Mo₂C@CN and Fe-Mo₂C@CN. It is observed in Fig. 6e that the metal d-band centre declines with the introduction of Fe. This suggests that the M-O

antibonding orbital is filled, the electron repulsion (U) within the d orbital increases, and the charge transfer energy (Δ) between the highly oxidized metal and oxygen decreases. Enabling the electron-filled lower Hubbard band (LHB) to penetrate into the O 2p band corresponds to the energy band diagram in Fig. 6f from left to right to explain. At this moment, the M-O robustness is weakened and electrons are transferred from the oxygen ligand to the TM cation in the lattice matrix, providing holes for lattice oxygen activation and making the lattice oxygen more susceptible to oxidation to participate in the OER reaction. The doping of Fe enables the material to strengthen the OER reaction thermodynamic process while weakening the M-O bond and activating the lattice oxygen to participate in LOM.

3.5. Electrocatalytic water splitting performance

To reflect the applicability of the material, it was assembled as an anode and a commercial Pt slice ($1 \times 1 \text{ cm}^2$) as a cathode to form a water splitting cell. Cell voltage reaches 1.526 V at a current density of 10 mA cm^{-2} , which is better than Pt||RuO₂ (1.561 V). Furthermore, Fig. 7a shows that the gap between the two cells becomes wider as the current density increases. Additionally, after a long time stability test,

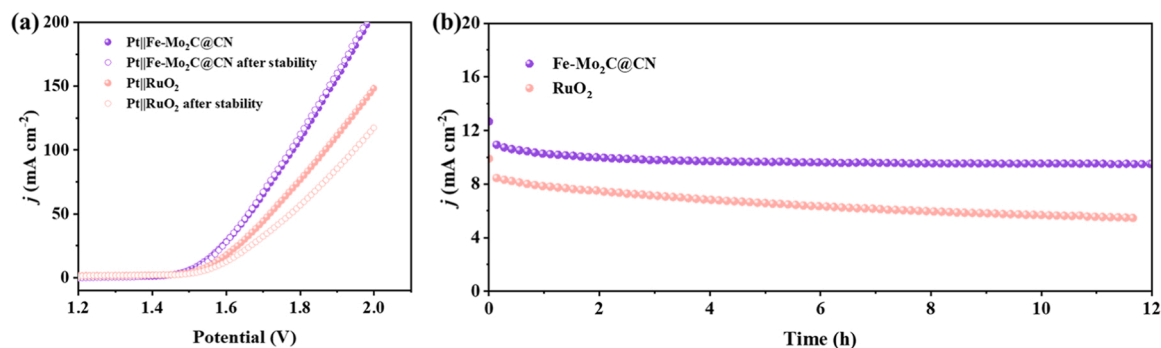


Fig. 7. (a) The comparison of LSV curves of Pt||Fe-Mo₂C@CN and Pt||RuO₂ cells and (b) stability curves.

the voltage of Pt||Fe-Mo₂C@CN cell can maintain a relatively stable state, and the slight fade is caused by the catalyst shedding, while Pt||RuO₂ undergoes a significant decay (Fig. 7b). It is significant to design a bifunctional electrocatalyst that can promote both HER and OER [40, 41]. Due to the HER potential of molybdenum carbide itself, it was used simultaneously as a cathode and anode for a water splitting cell (Fig. S20). The cell voltage reached 1.539 V with a current density of 10 mA cm⁻². This indicates that Fe-Mo₂C@CN has outstanding electrocatalytic potential for water splitting.

4. Conclusion

To sum up, we synthesized Fe-Mo₂C@CN with excellent electrocatalytic OER properties and verified that the OER process of the material conforms to the thermodynamically favorable single site LOM by incorporating experiments with theoretical calculations. The dual role of Fe in the material enhanced the OER process in terms of the kinetics and electronic structure of the material, respectively. Not only does the introduction of Fe reduce the dissolution of Mo and enhance the electrical conductivity of the material, but also it decreases the d-band center of the material causing the M-O antibonding orbitals to be filled, promotes the activation of lattice oxygen, and allows it to participate in the OER process. It also has excellent electrocatalytic performance and stability when applied as a water splitting full cell anode. This work lays the foundation for the reaction mechanism of Mo-based catalysts in the OER process and provides some insights into the discovery of other OER electrocatalysts based on LOM.

CRedit authorship contribution statement

Qingcui Liu: Conceptualization, Methodology, Formal analysis, Writing – original draft, Writing – review & editing. **Qiaohong Su:** Writing – review & editing. **Wenhua Cheng:** Writing – review & editing. **Juan Ding:** Writing – review & editing. **Wenjun Zhang:** Resources, Writing – review & editing. **Jiulin Wang:** Writing – review & editing. **Yonggang Wang:** Writing – review & editing, Supervision. **Xingchao Wang:** Writing – review & editing. **Yudai Huang:** Funding acquisition, Writing – review & editing, Supervision.

Declaration of Competing Interest

The authors declare that they have no known competing financial interests or personal relationships that could have appeared to influence the work reported in this paper.

Data availability

Data will be made available on request.

Acknowledgments

This work was financially supported by the National Natural Science Foundation of China (52162036, 21965034, U1903217, and 22065033), the Key Project of Nature Science Foundation of Xinjiang Province (2021D01D08), the Xinjiang Autonomous Region Major Projects (2022A01005–4 and 2021A01001–1). Shenzhen Huasuan Technology Co., Ltd. is acknowledged for their contribution to density functional theory (DFT) analysis.

Appendix A. Supporting information

Supplementary data associated with this article can be found in the online version at [doi:10.1016/j.apcatb.2023.123188](https://doi.org/10.1016/j.apcatb.2023.123188).

References

- [1] W. Wu, Y. Huang, X. Wang, P.K. Shen, J. Zhu, Composition-optimized manganese phosphide nanoparticles anchored on porous carbon network for efficiently electrocatalytic hydrogen evolution, *Chem. Eng. J.* 469 (2023), 143879, <https://doi.org/10.1016/j.cej.2023.143879>.
- [2] F. Guo, T.J. Macdonald, A.J. Sobrido, L. Liu, J. Feng, G. He, Recent advances in ultralow-pt-loading electrocatalysts for the efficient hydrogen evolution, *Adv. Sci.* 10 (2023), 2301098, <https://doi.org/10.1002/adv.202301098>.
- [3] M.J. Choi, L. Wang, K.A. Stoerzinger, S.Y. Chung, S.A. Chambers, Y. Du, Epitaxial design of complex nickelates as electrocatalysts for the oxygen evolution reaction, *Adv. Energy Mater.* 13 (2023), 2300239, <https://doi.org/10.1002/aenm.202300239>.
- [4] T. Zhang, J. Sun, J. Guan, Self-supported transition metal chalcogenides for oxygen evolution, *Nano Res.* 16 (2023) 8684–8711, <https://doi.org/10.1007/s12274-023-5670-6>.
- [5] H.H. Jiawei Shi, Yinghua Guo, Feng Ji, Jing Li, Yi Zhang, Chengwei Deng, Liyuan Fan, Weiwei Cai, Enabling high-efficiency ethanol oxidation on NiFe-LDH via deprotonation promotion and absorption inhibition, *J. Energy Chem.* 85 (2023) 76–82, <https://doi.org/10.1016/j.jechem.2023.06.011>.
- [6] S. Zhou, J. Wang, J. Li, L. Fan, Z. Liu, J. Shi, W. Cai, Surface-growing organophosphorus layer on layered double hydroxides enables boosted and durable electrochemical freshwater/seawater oxidation, *Appl. Catal. B: Environ.* 332 (2023), 122749, <https://doi.org/10.1016/j.apcatb.2023.122749>.
- [7] H. Wang, M. Gu, X. Huang, A. Gao, X. Liu, P. Sun, X. Zhang, Ligand-based modulation of the electronic structure at metal nodes in MOFs to promote the oxygen evolution reaction, *J. Mater. Chem. A* 11 (2023) 7239–7245, <https://doi.org/10.1039/D2TA09665J>.
- [8] W. Luo, Y. Yu, Y. Wu, Z. Ma, X. Ma, Y. Jiang, W. Shen, R. He, W. Su, M. Li, Realizing efficient oxygen evolution at low overpotential via dopant-induced interfacial coupling enhancement effect, *Appl. Catal. B: Environ.* 336 (2023), 122928, <https://doi.org/10.1016/j.apcatb.2023.122928>.
- [9] J. Song, C. Wei, Z.-F. Huang, C. Liu, L. Zeng, X. Wang, Z.J. Xu, A review on fundamentals for designing oxygen evolution electrocatalysts, *Chem. Soc. Rev.* 49 (2020) 2196–2214, <https://doi.org/10.1039/C9CS00607A>.
- [10] X. Wang, H. Zhong, S. Xi, W.S.V. Lee, J. Xue, Understanding of oxygen redox in oxygen evolution reaction, *Adv. Mater.* 34 (2022), 2107956, <https://doi.org/10.1002/adma.202107956>.
- [11] A. Grimaud, O. Diaz-Morales, B. Han, W.T. Hong, Y.L. Lee, L. Giordano, K. A. Stoerzinger, M. Koper, Y. Shao-Horn, Activating lattice oxygen redox reactions in metal oxides to catalyze oxygen evolution, *Nat. Chem.* 9 (2017) 457–465, <https://doi.org/10.1038/nchem.2695>.
- [12] R. He, M. Li, W. Qiao, L. Feng, Fe doped Mo/Te nanorods with improved stability for oxygen evolution reaction, *Chem. Eng. J.* 423 (2021), 130168, <https://doi.org/10.1016/j.cej.2021.130168>.

- [13] M. Ning, F. Zhang, L. Wu, X. Xing, D. Wang, S. Song, Q. Zhou, L. Yu, J. Bao, S. Chen, Z. Ren, Boosting efficient alkaline fresh water and seawater electrolysis via electrochemical reconstruction, *Energy Environ. Sci.* 15 (2022) 3945–3957, <https://doi.org/10.1039/d2ee01094a>.
- [14] S. Zhou, Y. Liu, J. Li, Z. Liu, J. Shi, L. Fan, W. Cai, Surface-neutralization engineered NiCo-LDH/phosphate hetero-sheets toward robust oxygen evolution reaction, *Green. Energy Environ.* (2022), <https://doi.org/10.1016/j.gee.2022.12.003>.
- [15] X. Yang, J. Cheng, X. Yang, Y. Xu, W. Sun, J. Zhou, Facet-tunable coral-like Mo₂C catalyst for electrocatalytic hydrogen evolution reaction, *Chem. Eng. J.* 451 (2023), 138977, <https://doi.org/10.1016/j.cej.2022.138977>.
- [16] Y. Chen, B. Gao, M. Wang, X. Xiao, A. Lv, S. Jiao, P.K. Chu, Dual-phase MoC-Mo₂C nanosheets prepared by molten salt electrochemical conversion of CO₂ as excellent electrocatalysts for the hydrogen evolution reaction, *Nano Energy* 90 (2021), 106533, <https://doi.org/10.1016/j.nanoen.2021.106533>.
- [17] F. Yu, L. Yu, I.K. Mishra, Y. Yu, Z.F. Ren, H.Q. Zhou, Recent developments in earth-abundant and non-noble electrocatalysts for water electrolysis, *Mater. Today Phys.* 7 (2018) 121–138, <https://doi.org/10.1016/j.mtphys.2018.11.007>.
- [18] E. Jiang, J. Li, X. Li, A. Ali, G. Wang, S. Ma, P. Kang Shen, J. Zhu, MoP-Mo₂C quantum dot heterostructures uniformly hosted on a heteroatom-doped 3D porous carbon sheet network as an efficient bifunctional electrocatalyst for overall water splitting, *Chem. Eng. J.* 431 (2022), 133719, <https://doi.org/10.1016/j.cej.2021.133719>.
- [19] Y.-T. Xu, Z.-M. Ye, J.-W. Ye, L.-M. Cao, R.-K. Huang, J.-X. Wu, D.-D. Zhou, X.-F. Zhang, C.-T. He, J.-P. Zhang, X.-M. Chen, Non-3d metal modulation of a cobalt imidazolate framework for excellent electrocatalytic oxygen evolution in neutral media, *Angew. Chem. Int. Ed.* 58 (2019) 139–143, <https://doi.org/10.1002/anie.201809144>.
- [20] S. Yuan, M. Xia, Z. Liu, K. Wang, L. Xiang, G. Huang, J. Zhang, N. Li, Dual synergistic effects between Co and Mo₂C in Co/Mo₂C heterostructure for electrocatalytic overall water splitting, *Chem. Eng. J.* 430 (2022), 132697, <https://doi.org/10.1016/j.cej.2021.132697>.
- [21] Y. Wang, L. Wang, M. Tong, X. Zhao, Y. Gao, H. Fu, Co-VN encapsulated in bamboo-like N-doped carbon nanotubes for ultrahigh-stability of oxygen reduction reaction, *Nanoscale* 10 (2018) 4311–4319, <https://doi.org/10.1039/C7NR09538D>.
- [22] Z.-N. Hu, Y. Ai, W. Xu, X. Zhang, Z. Sun, L. Guo, R. Guo, Y. Wang, K. Ding, H.-B. Sun, J. Hu, Q. Liang, Y. Yang, Iron catalyzed cascade construction of molybdenum carbide heterointerfaces for understanding hydrogen evolution, *Small* 18 (2022), 2200439, <https://doi.org/10.1002/smll.202200439>.
- [23] Z. Kou, L. Zhang, Y. Ma, X. Liu, W. Zang, J. Zhang, S. Huang, Y. Du, A.K. Cheetham, J. Wang, 2D carbide nanomeshes and their assembling into 3D microflowers for efficient water splitting, *Appl. Catal. B: Environ.* 243 (2019) 678–685, <https://doi.org/10.1016/j.apcatb.2018.11.008>.
- [24] C. Wan, Y.N. Regmi, B.M. Leonard, Multiple phases of molybdenum carbide as electrocatalysts for the hydrogen evolution reaction, *Angew. Chem. Int. Ed.* 53 (2014) 6407–6410, <https://doi.org/10.1002/ange.201402998>.
- [25] Y. Li, Z. Yin, X. Liu, M. Cui, S. Chen, T. Ma, Current progress of molybdenum carbide-based materials for electrocatalysis: potential electrocatalysts with diverse applications, *Mater. Today Chem.* 19 (2021), 100411, <https://doi.org/10.1016/j.mtchem.2020.100411>.
- [26] C. Wan, B.M. Leonard, Iron-doped molybdenum carbide catalyst with high activity and stability for the hydrogen evolution reaction, *Chem. Mater.* 27 (2015) 4281–4288, <https://doi.org/10.1021/acs.chemmater.5b00621>.
- [27] S. Li, B. Chen, Y. Wang, M.-Y. Ye, P.A. van Aken, C. Cheng, A. Thomas, Oxygen-evolving catalytic atoms on metal carbides, *Nat. Mater.* 20 (2021) 1240–1247, <https://doi.org/10.1038/s41563-021-01006-2>.
- [28] J. Xing, Y. Li, S. Guo, T. Jin, H. Li, Y. Wang, L. Jiao, Molybdenum carbide in-situ embedded into carbon nanosheets as efficient bifunctional electrocatalysts for overall water splitting, *Electrochim. Acta* 298 (2019) 305–312, <https://doi.org/10.1016/j.electacta.2018.12.091>.
- [29] L. Zhang, Y. Zhu, Z. Nie, Z. Li, Y. Ye, L. Li, J. Hong, Z. Bi, Y. Zhou, G. Hu, Co/MoC nanoparticles embedded in carbon nanoboxes as robust trifunctional electrocatalysts for a Zn-air battery and water electrocatalysis, *ACS Nano* 15 (2021) 13399–13414, <https://doi.org/10.1021/acsnano.1c03766>.
- [30] I.B. Sharma, D. Singh, Solid state chemistry of Ruddlesden-Popper type complex oxides, *Bull. Mater. Sci.* 21 (1998) 363–374, <https://doi.org/10.1007/bf02744920>.
- [31] G. Qian, J. Chen, T. Yu, J. Liu, L. Luo, S. Yin, Three-phase heterojunction nimo-based nano-needle for water splitting at industrial alkaline condition, *Nano-Micro Lett.* 14 (2021) 20, <https://doi.org/10.1007/s40820-021-00744-x>.
- [32] W. Wang, J. Wang, S. Zhang, X. Song, B. Ma, Engineering of surface metal-nitrogen moieties in Fe-V based hybrid electrocatalysts for enhanced water oxidation, *J. Mater. Chem. A* 10 (2022) 12334–12340, <https://doi.org/10.1039/D2TA02244C>.
- [33] Y. Pan, X. Xu, Y. Zhong, L. Ge, X. Chen, J.-P.M. Veder, D. Guan, R. O'Hayre, M. Li, G. Wang, H. Wang, W. Zhou, Z. Shao, Direct evidence of boosted oxygen evolution over perovskite by enhanced lattice oxygen participation, *Nat. Commun.* 11 (2020), 2002, <https://doi.org/10.1038/s41467-020-15873-x>.
- [34] J. Jiang, Q. Liu, C. Zeng, L. Ai, Cobalt/molybdenum carbide@N-doped carbon as a bifunctional electrocatalyst for hydrogen and oxygen evolution reactions, *J. Mater. Chem. A* 5 (2017) 16929–16935, <https://doi.org/10.1039/C7TA04893A>.
- [35] A. Moysiadou, S. Lee, C.S. Hsu, H.M. Chen, X. Hu, Mechanism of oxygen evolution catalyzed by cobalt oxyhydroxide: cobalt superoxide species as a key intermediate and dioxygen release as a rate-determining step, *J. Am. Chem. Soc.* 142 (2020) 11901–11914, <https://doi.org/10.1021/jacs.0c04867>.
- [36] N. Zhang, X. Feng, D. Rao, X. Deng, L. Cai, B. Qiu, R. Long, Y. Xiong, Y. Lu, Y. Chai, Lattice oxygen activation enabled by high-valence metal sites for enhanced water oxidation, *Nat. Commun.* 11 (2020) 4066, <https://doi.org/10.1038/s41467-020-17934-7>.
- [37] K. Liu, S. Tan, J. Moon, C.J. Jafta, C. Li, T. Kobayashi, H. Lyu, C.A. Bridges, S. Men, W. Guo, Y. Sun, J. Zhang, M.P. Paranthaman, X.-G. Sun, S. Dai, Insights into the enhanced cycle and rate performances of the F-substituted P2-type oxide cathodes for sodium-ion batteries, *ACS Omega* 10 (2020), 2000135, <https://doi.org/10.1002/aenm.202000135>.
- [38] S. Lee, L. Bai, X. Hu, Deciphering iron-dependent activity in oxygen evolution catalyzed by nickel-iron layered double hydroxide, *Angew. Chem. Int. Ed.* 59 (2020) 8072–8077, <https://doi.org/10.1002/anie.201915803>.
- [39] N. Zhang, Y. Chai, Lattice oxygen redox chemistry in solid-state electrocatalysts for water oxidation, *Energy Environ. Sci.* 14 (2021) 4647–4671, <https://doi.org/10.1039/D1EE01277K>.
- [40] X. Wang, G. Huang, Z. Pan, S. Kang, S. Ma, P.K. Shen, J. Zhu, One-pot synthesis of Mn₂P-Mn₂O₃ heterogeneous nanoparticles in a P, N-doped three-dimensional porous carbon framework as a highly efficient bifunctional electrocatalyst for overall water splitting, *Chem. Eng. J.* 428 (2022), 131190, <https://doi.org/10.1016/j.cej.2021.131190>.
- [41] G. Huang, M. Hu, X. Xu, A.A. Allothman, M.S.S. Mushab, S. Ma, P.K. Shen, J. Zhu, Y. Yamauchi, Optimizing Heterointerface of Co₂P-Co₃O₄ nanoparticles within a porous carbon network for deciphering superior water splitting, *Small Struct.* 4 (2023), 2200235, <https://doi.org/10.1002/ssr.202200235>.